Research Article | Vol. 33, No. 23 / 17 Nov 2025 / Optics Express 49016
Optics EXPRESS

Mid-wave infrared multi-order SPPs resonance by exciting multi-order diffractions in 1D Dammann gratings

ZHENGCHAO CHEN,[1,2] LIBIN TANG,[1,2,3,5] QUN HAO,[1,6] KAR SENG TENG,[4,7] CHAOQUN WEI,[2] SHICHUN XU,[2] AND BIAO YUE[2]

[1]The Laboratory of Photonics Information Technology, Ministry of Industry and Information Technology, School of Optics and Photonics, Beijing Institute of Technology, Beijing 100081, China
[2]Kunming Institute of Physics, Kunming 650223, China
[3]Yunnan Key Laboratory of Advanced Photoelectronic Materials & Devices, Kunming 650223, China
[4]Department of Electronic and Electrical Engineering, Swansea University, Bay Campus, Fabian Way, Swansea SA1 8EN, United Kingdom
[5]scitang@163.com
[6]qhao@bit.edu.cn
[7]k.s.teng@swansea.ac.uk

Abstract: Mid-wave infrared photodetectors offer significant potential for a wide range of important applications. Due to their unique sub-wavelength localization properties, infrared photodetectors based on surface plasmon polaritons (SPPs) have garnered considerable research interest. Many of these applications require bandwidth response from the infrared photodetectors. In this paper, Dammann gratings (DGs) with a one-dimensional (1D) metal/dielectric layer structure were designed to achieve a diffraction field distribution modulated by a non-sinc function, which in turn was used to excite SPPs resonance. These gratings are capable of supporting multi-order SPPs resonance, facilitating enhanced bandwidth absorption across multiple resonant orders. By varying the combinations of diffraction slit spacings within a single period, the DGs could achieve distinct phase difference distributions. Specifically, DGs with a lattice constant of $d = 27.3\,\mu m$ demonstrated the ability to generate two to four orders of strong diffraction intensity distribution within 4-5 μm range, thereby enabling multi-order resonance-enhanced absorption of SPPs. Furthermore, the SPPs response of the DGs exhibited improved tolerance to variations in polarization angles across a broadband spectrum. This multi-order SPPs resonance-enhanced structure presents significant potential for applications in infrared detection, including the development of large-scale infrared photodetector units.

1. Introduction

Mid-infrared (mid-IR; 2.5-25 μm) wavelengths have emerged as a pivotal range for a variety of applications, spanning from environmental monitoring to fundamental scientific research. Within this spectrum, the mid-wave infrared (MWIR; 3-5 μm) atmospheric transmission window is particularly significant, playing a vital role in infrared sensing, gas detection, and free-space optical communication [1,2]. Recent advancements in infrared detection technology have placed a strong emphasis on achieving higher operating temperatures, which is a key trend for developing high-performance cooled infrared photodetectors [3]. Utilizing a thin absorption layer is essential to facilitate these elevated operating temperatures. However, such thin designs can adversely affect the absorption efficiency of devices, particularly in infrared detectors like type-II superlattice and quantum dots, which are limited by factors such as carrier diffusion length and consequently also require thin absorption regions [4,5].

#577285 https://doi.org/10.1364/OE.577285
Journal © 2025 Received 1 Sep 2025; revised 27 Oct 2025; accepted 27 Oct 2025; published 11 Nov 2025

Optics EXPRESS

Surface plasmon polaritons (SPPs), known for their sub-wavelength localization, exhibit significant field enhancement at interfaces [6,7]. This enhancement leads to an increased photon density of states [8], which subsequently promotes enhanced light-matter interactions and increases light absorption within the material [2,9]. As a result, SPPs have been extensively studied in the field of optoelectronic detection [10–19].

SPPs are a distinct class of surface electromagnetic modes formed at the interface between metals and dielectrics, resulting from the coupling between incident electromagnetic waves and the oscillation of the free electron plasma in metals [20]. When SPPs propagate along the interface, the electric field component perpendicular to the interface exhibits exponential decay [21]. Given that the wave vector of SPPs (k_{spp}) is greater than that of free-space light (k_0), direct coupling between freely propagating light and SPPs is not possible. To overcome this limitation, wave vector compensation techniques must be employed, including methods such as prism coupling, grating coupling, and plasma micro-cavity coupling [20,22]. It is important to note that SPPs are characterized as evanescent waves. Thus, to enhance the absorption within a detector using SPPs, the detector must be positioned within the evanescent field [23,24]. By integrating two-dimensional (2D) perforated SPPs gratings arrays with devices such as InAs mid-wave infrared (MWIR) [19] and long-wave infrared (LWIR) [10] quantum dots, quantum cascades [25], and quantum wells [23], detectors can achieve significant coupling with the localized SPPs fields. Such integration substantially enhances the optical response. Infrared detectors based on nBn-type InAsSbs that are integrated with one-dimensional (1D) or 2D reflective SPPs gratings have been shown to enhance localized absorption effectively. Notably, these studies have demonstrated significant increases in quantum efficiency (QE), even with an absorption layer thickness as thin as 0.5 μm, highlighting the potential of SPPs to enhance QE in thin absorption layers [11,13,26,27].

In conventional 1D or 2D SPPs gratings, the unit cell typically consists of a diffraction slit. The intensity distribution resulting from periodic multi-slit interference is largely determined by the envelope of the sinc function, leading to an uneven intensity distribution across different diffraction orders. Specifically, lower diffraction orders tend to yield higher intensity and broader wavelength spacing when SPPs are excited, whereas higher diffraction orders exhibit weaker intensity and tighter wavelength spacing. This phenomenon places limits on resonance enhancement achievable within higher orders. Consequently, when using SPPs gratings to enhance absorption, lower diffraction orders are generally preferred due to their greater intensity. However, the narrow resonance bandwidth inherent to these individual orders limit the ability of conventional SPPs gratings to achieve broadband absorption. In contrast, a unit cell in a 2D hole array grating that contains two holes of different sizes has been found to yield two distinct resonance peaks in the response curve of a p-type InAs infrared detector, thereby broadening the response bandwidth [18].

Dammann gratings (DGs), similar to the grating mentioned above, are uniquely structured with multiple diffraction slits of varying widths arranged non-uniformly within a single period. Although the overall distribution remains periodic, the transmittance or reflectance within each period is non-periodic. This configuration enables the modulation of the intensity distribution of DGs by both intra-period and inter-period interference effects, resulting in a light intensity distribution that deviates from the sinc function [28]. Conventionally designed as efficient wavefront beam-splitting devices, DGs are optimized to produce a uniform array of diffraction orders with equal intensities at a single operational wavelength [28–31]. In this work, however, we identify and leverage a previously unexplored degree of freedom: when employed for the excitation of SPPs, a fixed DGs inherently supports multiple discrete resonance wavelengths. This arises from the precise phase-matching condition between the resonant wavelength of SPPs and the incident momentum provided by various diffraction orders. Consequently, the conventional functionality of wavelength-specific beam splitting is transformed into a novel

Optics EXPRESS

capacity for synchronous multi-wavelength, multi-order SPPs excitation. This approach opens up new avenues for spectral control in the mid-infrared regime and provides advanced design strategies for integrated photonic devices.

In this study, 1D reflective DGs with a metal/dielectric layer structure were designed and employed to excite SPPs. An analysis of the reflection spectrum revealed that the DGs successfully excited multi-order SPPs responses. Moreover, a comparative analysis of angular dispersion revealed that DGs exhibited superior tolerance to angular dispersion when compared with conventional gratings.

2. Numerical analysis and experiment

2.1. Numerical analysis methods

The light intensity distribution for each diffraction order of the DGs under normal incidence was computed using MATLAB software. Additionally, the 1D DGs were simulated using the Electromagnetic Waves, Frequency Domain (EWFD) interface in COMSOL Multiphysics to investigate their SPP response. Throughout all calculations, a fixed incident wavelength was maintained to ensure uniform diffraction angles across all orders.

2.2. Fabrication of one-dimensional reflective Dammann gratings

The fabrication of 1D DGs involved a series of techniques, such as laser direct writing (PicoMaster ATE-200), ion beam etching (Ion Beam Etching, IBE), and magnetron sputtering (DISCOVERY635). Initially, a double-polished, high-resistance monocrystalline silicon wafer with a thickness of 0.5 mm was thoroughly cleaned using anhydrous ethanol. Following this, photoresist was spin-coated onto the wafer and baked on a hot plate at 90 °C for 120 s. Laser direct writing was performed on the substrate and then followed by annealing at 90 °C for 15 s. The exposed areas were developed using tetramethylammonium hydroxide solution for 45 s, after which the substrate was annealed again at 80 °C for 300 s. Next, the substrate was transferred to the ion beam etching equipment, where the silicon wafer was etched for 5 min under a vacuum of 6.5×10^{-4} Pa. Subsequently, the substrate was immersed in acetone for ultrasonic cleaning to remove any remaining photoresist and was dried using nitrogen gas. Finally, chromium (Cr) and gold (Au) layers were deposited onto the substrate using the magnetron sputtering technique under a vacuum of 5.0×10^{-6} mbar.

2.3. Structural and optical characterization

The Bruker INVENIO X FT-IR spectrometer, equipped with a non-polarized light source and its A519 accessory, was used to measure both the angle-independent reflection spectrum and the angular dispersion curve. During angular dispersion measurement, baseline correction was applied to the reflection spectrum. The morphology of the DGs was characterized using a scanning electron microscope (NOVA200 NANOSEM).

3. Results and discussion

3.1. Fraunhofer diffraction of Dammann gratings

The structure of one period of DGs is illustrated in Fig. 1(a). It is evident that the spectrum of the grating is entirely determined by the coordinates of the mutation points $\{b_m, c_m\}$ (where $m = 1, 2\ldots, L$), with L representing the number of diffraction slits. The Fraunhofer diffraction light path of DGs is depicted in Fig. 1(b). In the x-direction, the width of each diffraction slit within a period is denoted as a_i (where $i = 1, 2\ldots, L$). The single-slit diffraction factor is expressed as $(\sin\alpha_i/\alpha_i)$, where $\alpha_i = \pi a_i \sin\theta/\lambda$, with λ being the wavelength of light and θ the diffraction angle. Considering N periods, we define the phase of the complex amplitude at point P on the

Optics EXPRESS

diffraction screen produced by the slit at the edge of the first period as $\delta_0 = 0$. The center position of the slits is represented as x_j (where $j = 1, 2\ldots, L$). Therefore, the phase difference at point P between adjacent diffraction slits can be calculated as $\delta_j = 2\pi(x_{j+1} - x_j)\sin\theta/\lambda = 2\beta_j'$. The phase difference between the first slit of the first period and the first slit of the second period is given by $\delta = 2\pi d\sin\theta/\lambda = 2\beta$. The total complex amplitude at point P on the observation screen can be expressed as follows:

$$E(P) = E_0 \frac{sinN\beta}{sin\beta} e^{i(N-1)\beta} \sum_{m=1}^{L} \frac{a_m}{a_1} \frac{sin\alpha_m}{\alpha_m} e^{i\sum_{j=0}^{m-1}\delta_j}, \tag{1}$$

where, E_0 represents the amplitude generated by the first slit at point P, while $\sin(N\beta)/\sin\beta$ denotes the inter-period multi-slit interference factor. The intensity of light at point P is given by $I = E(P)\cdot E(P)^*$.

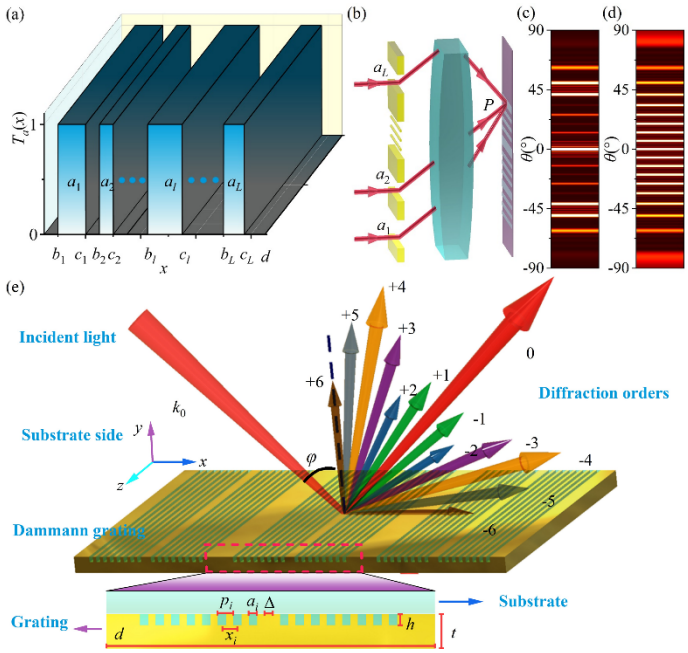

Fig. 1. (a) Schematic representation of 1D amplitude-type structure of DGs. (b) Fraunhofer diffraction pattern of DGs. (c) Diffraction Moiré fringes produced by DGs. (d) Diffraction Moiré fringes from conventional gratings for comparison, highlighting differences in pattern formation. (e) Schematic illustration depicting the structural parameters of the DGs.

The phase difference at point P on the observation screen between two diffraction slits depends on the center distance. By changing the center distance, the diffraction characteristics of DGs can be customized. If the widths of all diffraction slits within a period and the center distances between adjacent slits are equal, we have $\alpha_i = \pi a_i \sin\theta/\lambda = \alpha$ (where $i = 1, 2\ldots, L$) and $p = (x_{j+1} - x_j)$ (where $j = 1, 2, \ldots, L - 1$). Under these conditions, the diffraction slits in each period form a uniformly spaced conventional grating, and the above expression can be simplified to:

$$E(P) = E_0 \frac{sinN\beta}{sin\beta} \frac{sinL\beta'}{sin\beta'} \frac{sin\alpha}{\alpha} e^{i(N-1)\beta + i(L-1)\beta'}. \tag{2}$$

Consequently, the formula for the intensity of the diffracted light can be expressed as:

$$I = I_0 \left(\frac{sinN\beta}{sin\beta}\right)^2 \left(\frac{sinL\beta'}{sin\beta'}\right)^2 \left(\frac{sin\alpha}{\alpha}\right)^2, \tag{3}$$

Optics EXPRESS

where $I_0 = |E_0|^2$ is the light intensity produced by the first diffraction slit at point P.

In contrast to conventional gratings, the diffraction intensity of DGs is influenced by three primary factors: the single-slit diffraction factor $(\sin\alpha/\alpha)^2$, the inter-period multi-slit interference factor $(\sin(N\beta)/\sin\beta)^2$, and the intra-period multi-slit interference factor $(\sin(L\beta')/\sin\beta')^2$. This highlights that the diffraction intensity in DGs arises from the synergistic interplay of single-slit diffraction, intra-period multi-slit interference, and inter-period multi-slit interference. As a result, the diffraction field produced by the gratings demonstrates an intensity distribution that departs from the conventional sinc function, as illustrated in Fig. 1(c) and 1(d).

As a typical binary optical element, DGs exhibit mathematical equivalence between phase and amplitude modulation in their diffraction fields. Theoretically, an amplitude-modulated transmission grating model is adopted for design, while experimentally, a metallic rectangular reflective phase grating is fabricated to enhance diffraction efficiency while preserving the binary phase structure, as illustrated in Fig. 1(e). Meanwhile, the reflective (substrate-incident) configuration employed in this study is process-compatible with gratings fabricated via epitaxial technology, allowing direct integration atop the device [11,13]. For devices such as spin-coated quantum dot films, the grating surface can be directly coated and spin-coated, enabling air-side incidence while preserving the reflective modulation functionality of the grating.

3.2. Numerical analysis of SPPs response of Dammann gratings

The resonance wavelength of is designed to be 4–5 μm, with its specific value determined collectively by the plasmonic material, detector response band, and grating period. In shorter wavelength bands such as short-wave infrared (SWIR), detectors generally achieve high signal-to-noise ratios without the need for deep cooling. Moreover, conventional metals like Au and Ag exhibit stronger field localization capability, which facilitates enhanced field intensity. However, grating fabrication becomes more challenging. In mid- to long-wave infrared regions, deep cooling can improve detector signal-to-noise ratio, and larger gratings are easier to fabricate. Nevertheless, traditional metallic plasmonic materials exhibit weakened confinement of electromagnetic fields, leading to reduced localized enhancement performance. The performance in this regime can therefore be enhanced by adopting novel long-wave plasmonic materials, as evidenced by studies on heavily doped semiconductors [32–35].

The Bragg coupling condition for 1D SPPs gratings is defined by the equation [36]: $k_{spp} = 2\pi l/d \pm k_0 {\varepsilon_d}^{1/2} \sin\varphi$, where $k_0 = \omega/c$ represents the wave vector of light in a vacuum, $\varepsilon_d = {n_d}^2$ denotes the dielectric constant of the medium layer, φ signifies the angle of incidence, d is the period of the grating, and l is an integer indicating the diffraction order. The resonance wavelength necessary to excite SPPs can be expressed as:

$$\lambda_l = \frac{d}{l}\left(\sqrt{\frac{\varepsilon_m \varepsilon_d}{\varepsilon_m + \varepsilon_d}} \pm \sqrt{\varepsilon_d} sin\varphi\right), \tag{4}$$

where $\varepsilon_m = \varepsilon' + i\varepsilon''$ represents the complex dielectric constant of the metal.

In the mid-wave infrared range of 3-5 μm, commonly utilized plasmonic materials, such as gold and silver, exhibit a significantly large negative real part of the permittivity, typically satisfying $|\mathrm{Re}\{\varepsilon_m\}| >> \varepsilon_d$. Consequently, for normally incident light, the SPPs resonance wavelength can be approximated by $\lambda_l \approx d n_d/l$. The 1D DGs under investigation, as illustrated in Fig. 1(e), consist of 1D rectangular reflective gratings. The substrate of the gratings is composed of a gold layer [37] with a thickness (t) that significantly exceeds the skin depth, ensuring negligible transmission and thereby guaranteeing reflectance $R = 1 - A$, where A is the absorption coefficient. The lattice constant of the gratings is denoted by d, and monocrystalline silicon with a refractive index $n_{Si} = 3.4$ is selected as the dielectric material, assuming negligible absorption. For subsequent analyses, transverse magnetic (TM) plane waves are employed to illuminate the structures to evaluate their optical response. Initially, we consider normal incidence propagating along the

Optics EXPRESS

-y axis, where $\varphi = 0°$ and the electric field is polarized along the x-axis. Within each period, the diffraction slits are divided into two distinct regions, designated Region I and Region II, separated by an interval Δ. For analytical simplicity, each region contains $L/2$ diffraction slits, with equal spacing between the slits. Specifically, the slit spacing in Region I is denoted as $p_i = p_{\mathrm{I}}$ (where $i = 1, 2\ldots, L/2$), and in Region II as $p_j = p_{\mathrm{II}}$ (where $j = L/2+1, L/2+2\ldots, L$). The width of each slit a_i is uniformly set to 0.7 μm for all slits (where $i = 1, 2\cdots, L$). The lattice constant and the number of periods of the DGs are set at $d = 27.3$ μm and $N = 20$, respectively. Within the spectral range of 4-5 μm, five diffraction orders are observed: $\lambda_{19} \approx 4.89$ μm, $\lambda_{20} \approx 4.64$ μm, $\lambda_{21} \approx 4.42$ μm, $\lambda_{22} \approx 4.22$ μm, and $\lambda_{23} \approx 4.04$ μm. In subsequent analyses, we investigate how varying parameters such as the number of diffraction slits L, the distances p_{I} and p_{II}, and the interval Δ impact the SPPs response.

First, we set $p_{\mathrm{I}} = p_{\mathrm{II}} = 1.3$ μm, $\Delta = 0$ μm, and $L = 8$. Under these conditions, the diffraction slits within each period form a 1D grating array with a period of $p = 1.3$ μm. The conditions for generating diffraction orders from the gratings and the principal maxima resulting from intra-period multi-slit interference are given by $d\sin\theta = l\cdot\lambda$ (where $l = 0, \pm 1, \pm 2\ldots$) and $p\sin\theta = l'\cdot\lambda$ (where $l' = 0, \pm 1, \pm 2\ldots$), respectively. For normal incidence, the SPPs resonant modes excited by the diffraction orders of $+l$ and $-l$ are degenerate, allowing the incident light to couple into SPPs modes with identical electric field polarization E. For simplicity, we only illustrate the diffraction orders of $+l$ from 0° to 90° in the diffraction intensity distribution graph. The intensity distributions for the diffraction orders of the gratings are illustrated in Fig. 2(a) and (b). When $d/p = l/l'$, the diffraction angle θ of the principal maxima of intra-period multi-slit interference aligns with that of the diffraction orders of the gratings, as exemplified by the +21-diffraction order shown in Fig. 2(b). In contrast to conventional gratings, the modulation produced by intra-period multi-slit interference in the DGs results in an intensity distribution for each diffraction order that deviates from a sinc function. The principal maxima of the intra-period multi-slit interference exhibit a broader diffraction angle, thereby encompassing multiple diffraction orders and allowing for significant diffraction intensity, reminiscent of a band-pass filter effect. Meanwhile, other diffraction orders are modulated by secondary maxima of the intra-period multi-slit interference, leading to reduced diffraction intensity.

In the wavelength range of 3-5 μm, the absorption and reflection spectra of the DGs are presented in Fig. 2(c) to (e). The diffraction orders ranging from ±19 to ±22 generate surface evanescent waves that excite SPPs, resulting in dips in the zero-order reflection spectrum. Consequently, within the 4-5 μm range, the absorption curve reveals five distinct resonant absorption peaks. The intensity of these peaks is modulated by the intra-period multi-slit interference factor $(\sin(L\beta')/\sin\beta')^2$, where the central resonant peak exhibits the highest absorption intensity, while the edge peaks display lower intensity. Aside from the zero-order diffraction ($l = 0$), the gratings' diffraction intensity of light is predominantly distributed among $l = \pm 1, \pm 2$, and ±19 to ±22, showcasing notable differences when compared to the diffraction intensity distribution of conventional gratings.

Figure 2(e) shows the reflection spectra for $l = +1$ and +2 in the 4.6 to 4.8 μm wavelength range, which exhibit a Fano-like line shape. This asymmetric profile indicates interference between continuous and discrete states. Figure 2(f) and (g) depict how alterations in the slit width (a) and depth (h) influence the resonant absorption peaks of the DGs. Changes in these parameters influence only the wavelength position and half-width of the resonant peaks, without affecting their number.

The diffraction intensities of the DGs as a function of the number of slits L are illustrated in Fig. 2(h) and (i). As L increases, both the angular width of the principal maxima, due to intra-period multi-slit interference, and the number of observable diffraction orders decrease. Most diffraction intensity couples to the diffraction orders of $l = 0$ and $l = +21$. To ensure adequate diffraction efficiency, it is crucial to have a sufficient number of slits within each

Optics EXPRESS

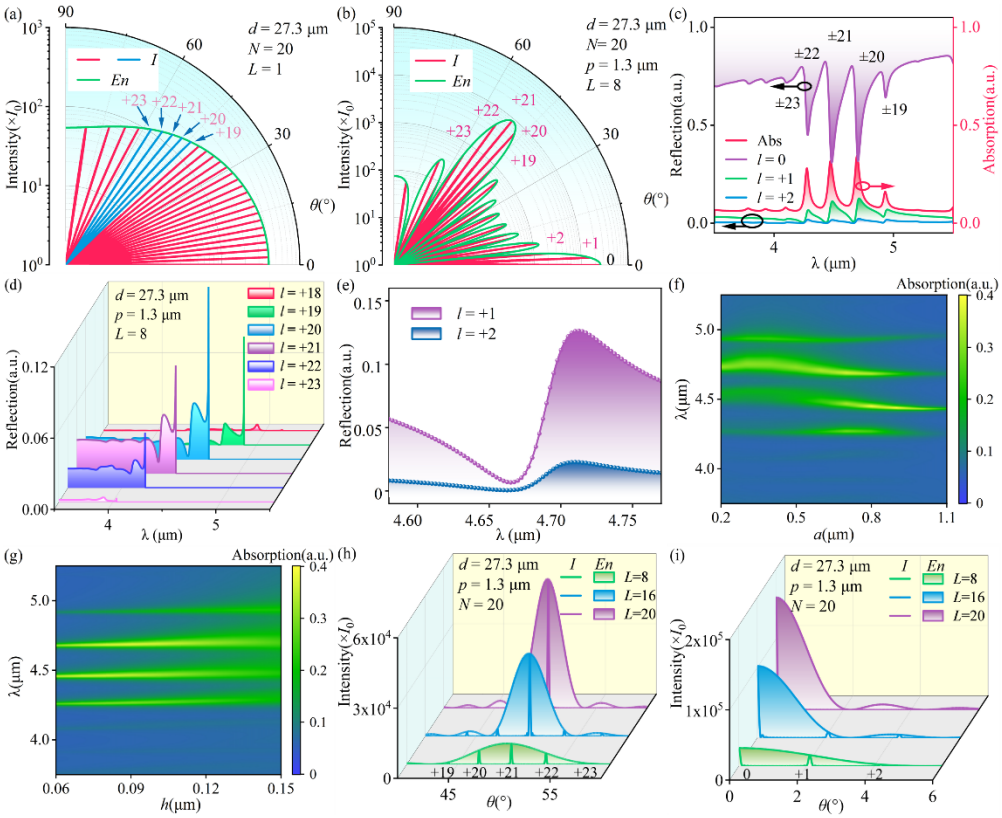

Fig. 2. (a),(b) Intensity distribution of the diffraction orders for conventional grating and DGs. The envelope curve *En* for the diffraction orders of the DGs is calculated using $I_0N^2(\sin L\beta'/\sin\beta')^2(\sin\alpha/\alpha)^2$. (c)-(e) Simulated curves illustrating the absorption and intensity of diffraction orders when $L = 8$ within a period. (f),(g) Effects of the slit width a and slit depth h on the resonance peaks of the DGs. (h),(i) Variations in light intensity at each diffraction order when taking different values of slit number L.

grating period. Maintaining other parameters constant, we configure the number of slits L to 16 and investigate slit spacing values of $p = 1.2\,\mu m$, $1.4\,\mu m$, and $1.5\,\mu m$. Figure 3(a) illustrates the intensity distribution across all diffraction orders. When $p \neq 1.3\,\mu m$, the diffraction angle corresponding to the intra-period multi-slit interference principal maximum of $l' = +1$ does not align with those of the DGs' diffraction orders. For $p = 1.4\,\mu m$, the diffraction order l of the DGs, corresponding to the principal maximum diffraction angle θ for $l' = +1$, is calculated as $l = l'\,(d/p) = 27.3/1.4 \approx 19.5$. This implies that the principal maximum diffraction angle θ of $l' = +1$ lies between the diffraction angles associated with the orders $l = +19$ and $l = +20$. These DG diffraction orders fall within the diffraction angular range of the principal maximum of $l' = +1$, symmetrically positioned at either end. This configuration ensures substantial diffraction intensity for both orders. For $p = 1.2\,\mu m$ and $1.5\,\mu m$, the diffraction orders l are approximately 22.75 and 18.2, respectively. The principal maxima corresponding to $l' = +1$ align more closely with $l = +23$ and $l = +18$, thus enhancing the diffraction intensity for these specific orders.

For $L = 16$, the DGs can achieve up to two significant diffraction orders when selecting different slit spacing values p. Although the diffraction angular range of the principal maxima $l' = +1$ can accommodate a maximum of three diffraction orders, only the central order exhibits

Optics EXPRESS

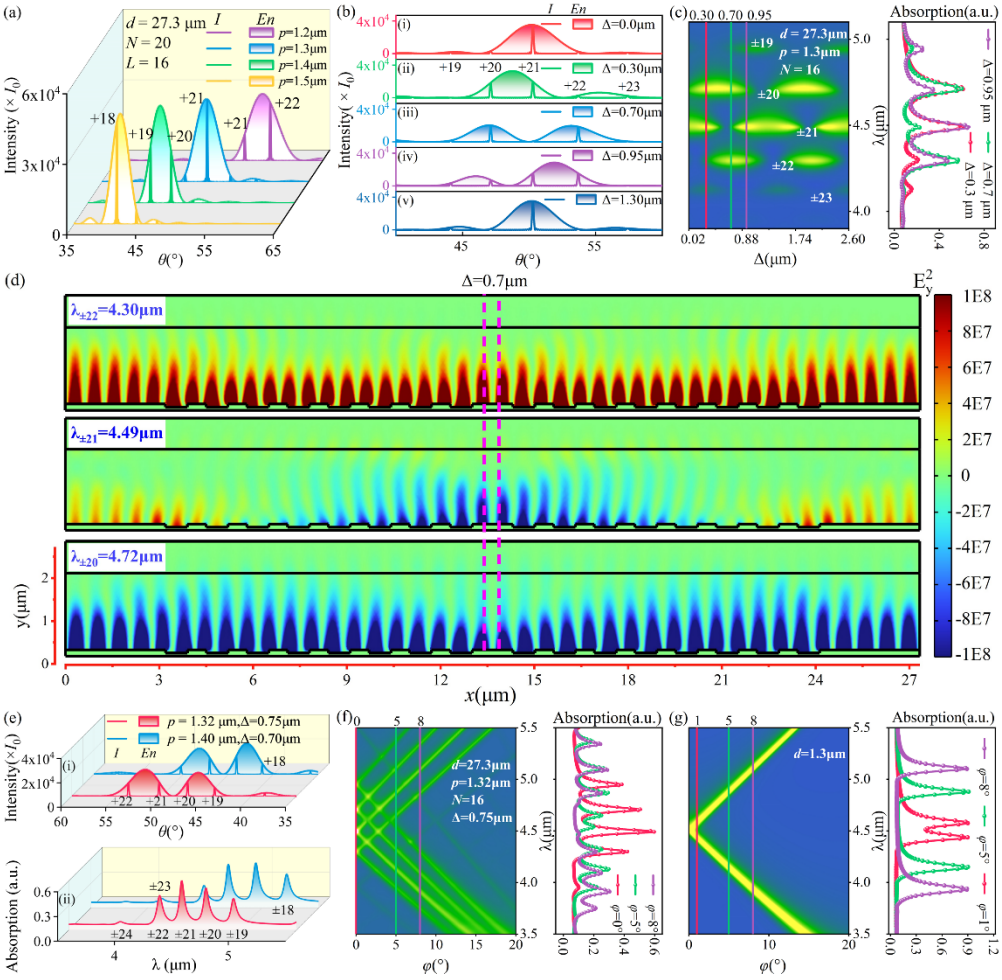

Fig. 3. (a) Diffraction intensity of DGs for the order $l' = +1$ as a function of p. (b),(c) Variations in diffraction intensity and absorption as a function of Δ for $L = 16$ and $p = 1.3$μm. (d) Distribution of E_y^2 at Δ=0.7μm. (e) Diffraction intensity and absorption curves for $p = 1.32$μm/Δ=0.75μm and $p = 1.4$μm/Δ=0.7μm. (f),(g) Dispersion characteristics of DGs and conventional gratings, respectively.

Optics EXPRESS

significant diffraction intensity. The intensities of the outer orders are suppressed by the function $(\sin L\beta'/\sin\beta')^2$, as shown for $p = 1.3$ μm in Fig. 3(a).

Furthermore, while maintaining a slit spacing of $p = 1.3$ μm in regions I and II, additional spacing is introduced between the two regions, which induces a phase difference. The resulting diffraction intensity distributions of the grating are illustrated in Fig. 3(b). When the spacing between the regions is set to $\Delta = 1.3\,m$ μm (where $m = 1, 2$), the phase difference between all diffraction slits within the period remains an integer multiple of $2\pi p\sin\theta/\lambda$ (with $p = 1.3$ μm). The diffraction intensity distributions of the DGs show characteristics similar to those observed at $\Delta = 0$, with predominant coupling of diffraction intensity into the $l = +21$ order. For Δ values of 0.3 μm, 0.7 μm, and 0.95 μm, the introduction of a phase difference significantly alters the diffraction intensity distributions across the diffraction orders. Specifically, at $\Delta = 0.3$ μm, the diffraction intensity predominantly couples to $l = +20$ and +21; at $\Delta = 0.7$ μm, it primarily couples to $l = +20$ and +22, with a notable suppression of the intensity of the $l = +21$ order; and at $\Delta = 0.95$ μm, the diffraction intensity couples to $l = +21$ and +22. The absorption spectra of SPPs response to the gratings vary with Δ, as illustrated in Fig. 3(c) to (d), with the distribution of resonant peaks aligning with changes in diffraction order intensity. For $p = 1.3$ μm, varying Δ allows the DGs to increase diffraction intensity by three orders of magnitude. Additionally, when p is set to 1.32 μm or 1.4 μm, adjusting Δ enables the gratings to enhance diffraction intensity by four orders of magnitude, as shown in Fig. 3(e).

In practical applications, the performance of incident light at oblique angles is a critical parameter. Thus, we select structural parameters $p = 1.32$ μm and $\Delta = 0.75$ μm for a detailed analysis. The number of slits per period is set to $L = 16$, and the angle of incidence φ varies from 0° to 20°. These results are compared with those of a conventional grating characterized by parameters $d = 1.3$ μm and $a = 0.7$ μm, as illustrated in Fig. 3(f) to (g). At $\varphi = 0°$, the conventional grating exhibits a single resonant peak within the 4-5 μm range. According to Eq. (4), as the angle of incidence increases, the two degenerate resonant peaks begin to separate. At $\varphi = 8°$, the split resonant absorption peaks shift beyond the 4-5 μm range. In contrast, the spectral analysis of the DGs reveals multiple resonant absorption peaks. When the higher-order resonant peak of the $+(l + 1)$ order intersects with the lower-order resonant peak of the $-(l - 1)$ order at $\varphi \neq 0°$, resonant absorption is significantly enhanced. Remarkably, at $\varphi = 8°$, the DGs can still achieve three distinct resonant absorption peaks within the 4-5 μm range.

3.3. Experimental verification

In this study, four distinct DGs samples were fabricated and tested to evaluate their performance against that of conventional gratings, thereby validating the proposed method. The detailed fabrication process for the DGs is illustrated in Fig. 4(a). SEM images, presented in Fig. 4(b) to (e), show the structural characteristics of the fabricated DGs. During the fabrication process, the etching linewidth on the silicon substrate was meticulously controlled to a precise measurement of 1 μm. For periods of $p = 1.4$ μm and 1.5 μm, the designed slit widths a were specified as 400 nm and 500 nm, while the actual measured slit widths were found to be 448 nm and 527 nm, respectively. This demonstrates a strong correlation between the theoretical and actual structural parameters. The metal layer was composed of a 6 nm Cr adhesion layer and a 200 nm Au conductive layer.

The resonance wavelength observed during the testing process is influenced by both the incident angle φ and the azimuthal angle γ. The Bragg coupling condition can be expressed as $k_{spp} = 2\pi l/d \pm k_0 \varepsilon_d{}^{1/2}\sin\varphi\cdot\cos\gamma$, as illustrated in Fig. 4(f). When the samples are mounted on the reflection module stage of the spectrometer, the angle γ is non-zero and remains constant throughout the measurement process. By varying the incident angle φ, the degenerate SPPs propagating in the $+x$ and $-x$ directions experience a splitting effect, resulting in two distinct reflection dips in the reflection spectrum. For the case where $\gamma = 90°$, the Bragg coupling

Optics EXPRESS

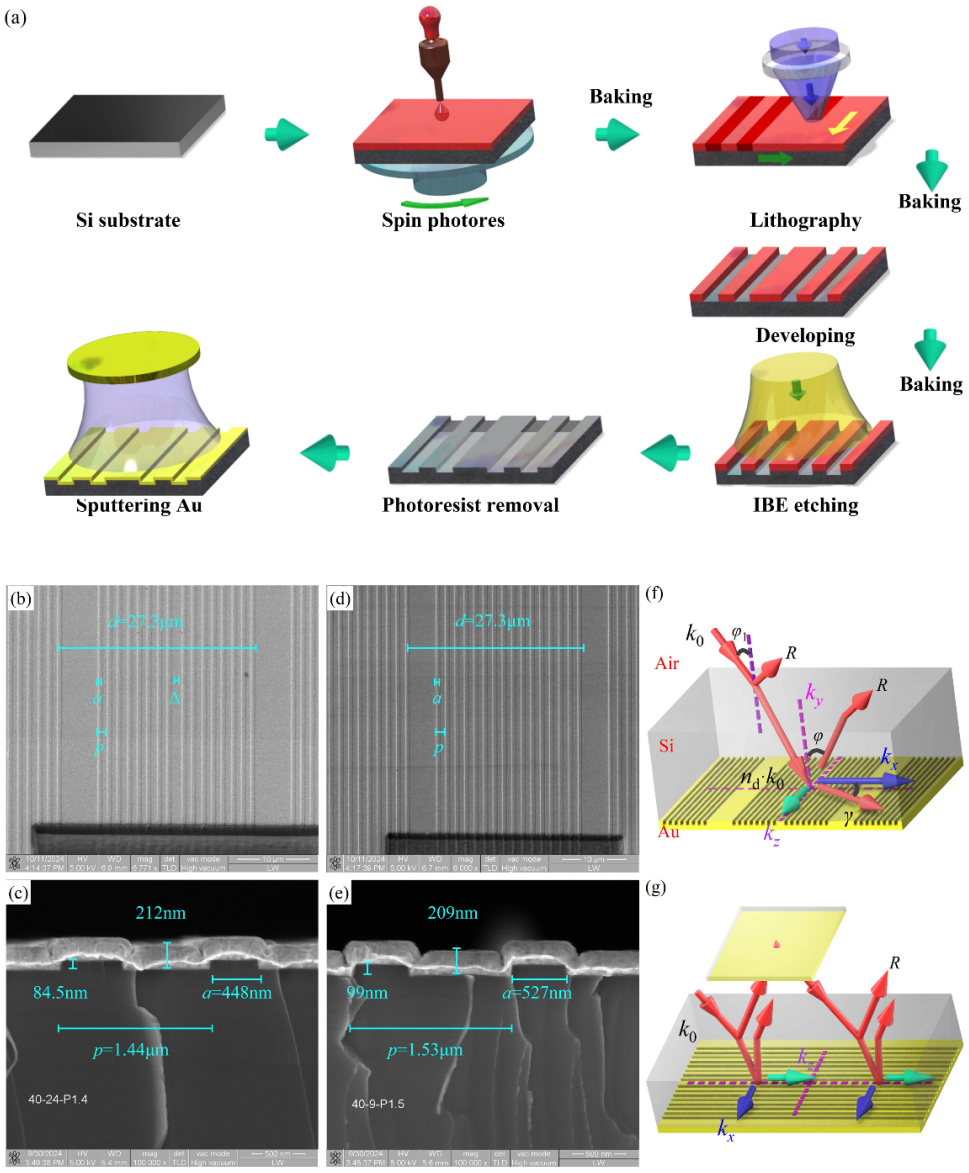

Fig. 4. (a) Overview of the fabrication process of DGs. (b)-(e) SEM images of the DGs. (f) Schematic diagram illustrating the dispersion characteristics of the DGs. (g) Optical path of reflective spectrum measurement at γ=90 °.

condition simplifies to $k_{spp} = 2\pi l/d$. In this configuration, although the incident angle φ is greater than 0°, there is no component of the incident light wave vector along the grating periodic direction due to its 1D nature. Consequently, the SPPs response spectra of the gratings are similar to that observed under normal incidences, as illustrated in the optical path diagram in Fig. 4(g). The reflection spectra for the four 1D DGs at γ=90° are presented in Fig. 5(a) and (b). For the configurations of $p = 1.4\,\mu m/\Delta$=0 μm and $p = 1.5\,\mu m/\Delta$=0 μm, there are two and one resonance peaks, respectively. In contrast, the configurations of $p = 1.4\,\mu m/\Delta$=0.7 μm and $p = 1.32\,\mu m/\Delta$=0.75 μm display four distinct resonance peaks. Figure 5(b) includes a theoretical

Optics EXPRESS

simulation of the reflection spectrum for $p = 1.4\,\mu m/\Delta=0.7\,\mu m$, which is in agreement with the experimental data regarding both the number of reflection dips and the positions of the resonance wavelengths.

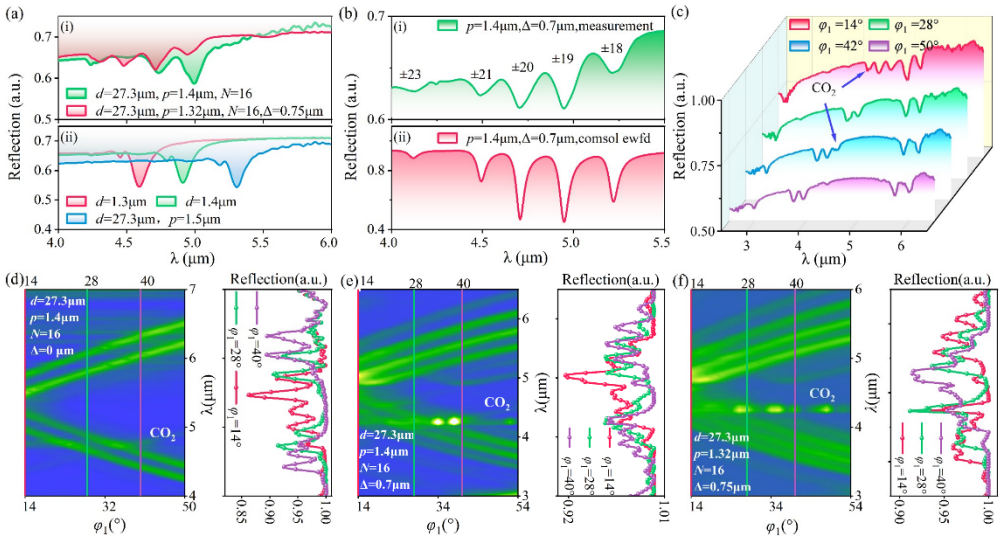

Fig. 5. (a),(b) Reflection spectra of DGs and conventional gratings. (c) Reflection spectra at different incident angles when $p = 1.4\,\mu m/\Delta=0\,\mu m$. (d)-(f) Dispersion characteristics of the DGs.

It is challenging to achieve an exact $\gamma = 90°$ during measurements. When the incident angle φ is not 0°, the degenerate resonance peaks may split. To confirm that the multiple resonance peaks observed in the DGs represent distinct resonance orders rather than merely splitting of degenerate resonances of the same order, a thorough analysis of the dispersion characteristics of the gratings was performed, as illustrated in Fig. 5(c) to (f). In this analysis, the incident angle φ_1 measured by the spectrometer corresponds to the incident angle at the silicon/air interface, while the angle φ at the metal/silicon interface is derived from φ_1 using Snell's law, illustrated in Fig. 4(f). For the DGs with $p = 1.32\,\mu m$ and $\Delta = 0.75\,\mu m$, when $\varphi_1 = 14°$, the reflection spectrum reveals four distinct reflection dips. As the angle increases, two of these dips shift towards longer wavelengths, while the other two shift towards shorter wavelengths, which is in agreement with the numerical data as illustrated in Fig. 3(f). The reflection dips that shift in the same direction correspond to different grating diffraction orders exciting the SPPs.

Due to the limitations of the variable-angle reflection measurement module of the spectrometer, the dispersion measurement range is confined to angles between 14° and 54°. In the reflection spectra of the three samples, a variable number of reflection dips are observed, confirming the effective excitation of SPPs by the incident light. The number of observed resonance peaks aligns with theoretical predictions, thereby validating the accuracy of the numerical analysis results.

4. Conclusion

In conclusion, DGs with a metal/dielectric layer structure have been successfully designed, achieving a diffraction light field distribution modulated by a non-sinc function. These gratings effectively excite SPPs, as demonstrated by experimental analyses of the reflection spectrum, which confirm the successful excitation of multi-order SPP resonances. An investigation into the dispersion characteristics of the DGs reveals three distinct resonance absorption peaks within the

Optics EXPRESS

4-5 μm spectral range at an incident angle of φ=8°, without accounting for refraction effects at the silicon/air interface. When refraction effects at the air/dielectric layer interface are considered, the DGs exhibit enhanced dispersion tolerance, indicating a superior performance compared to conventional gratings. Furthermore, the proposed multi-order SPPs resonance-enhanced absorption grating structure does not require a resonant cavity, thereby facilitating seamless integration with existing detector architectures. This innovative design presents significant potential for infrared detection applications, especially in developing large-size unit detectors.

Funding. National Key Research and Development Program of China (2019YFB2203404); Yunnan Province Innovation Team Project (2018HC020).

Disclosures. The authors declare no conflicts of interest.

Data availability. Data underlying the results presented in this paper are not publicly available at this time but may be obtained from the authors upon reasonable request.

References

1. X. Yang, Z. Sun, T. Low, *et al.*, "Nanomaterial-Based Plasmon-Enhanced Infrared Spectroscopy," Adv. Mater. **30**(20), e1704896 (2018).
2. R. Chang, H. Yang, Z. Wu, *et al.*, "Recent advances in mid-infrared photodetection based on colloidal quantum dots: Challenges and possible solutions," Coord. Chem. Rev. **500**(2020), 215539 (2024).
3. R. K. Bhan and V. Dhar, "Recent infrared detector technologies, applications, trends and development of HgCdTe based cooled infrared focal plane arrays and their characterization," Opto-Electron. Rev. **27**(2), 174–193 (2019).
4. T. H. Dang, M. Cavallo, A. Khalili, *et al.*, "Multiresonant Grating to Replace Transparent Conductive Oxide Electrode for Bias Selected Filtering of Infrared Photoresponse," Nano Lett. **23**(18), 8539–8546 (2023).
5. A. Kamboj, L. Nordin, P. Petluru, *et al.*, "All-epitaxial guided-mode resonance mid-wave infrared detectors," Appl. Phys. Lett. **118**(20), 201102 (2021).
6. J. A. Dionne and H. A. Atwater, "Plasmonics: Metal-worthy methods and materials in nanophotonics," MRS Bull **37**(8), 717–724 (2012).
7. F. Mao, J. Xie, S. Xiao, *et al.*, "Plasmonic light harvesting for multicolor infrared thermal detection," Opt. Express **21**(1), 295–304 (2013).
8. H. Wang, J. Xu, and Z. An, "Application of surface plasmon polariton grating in high sensitive infrared detectors," Sci. Sin. Phys. Mech. Astron. **49**(12), 124202 (2019).
9. M. D. Goldflam, E. A. Kadlec, B. V. Olson, *et al.*, "Enhanced infrared detectors using resonant structures combined with thin type-II superlattice absorbers," Appl. Phys. Lett. **109**(25), 251103 (2016).
10. C.-C. Chang, Y. D. Sharma, Y.-S. Kim, *et al.*, "A surface plasmon enhanced infrared photodetector based on InAs quantum dots," Nano Lett. **10**(5), 1704–1709 (2010).
11. E. M. Jackson, J. A. Nolde, M. Kim, *et al.*, "Two-dimensional plasmonic grating for increased quantum efficiency in midwave infrared nBn detectors with thin absorbers," Opt. Express **26**(11), 13850–13864 (2018).
12. J. Tong, L. Y. M. Tobing, S. Qiu, *et al.*, "Room temperature plasmon-enhanced InAs 0.91 Sb 0.09 -based heterojunction n-i-p mid-wave infrared photodetector," Appl. Phys. Lett. **113**(1), 11110 (2018).
13. J. A. Nolde, M. Kim, C. S. Kim, *et al.*, "Resonant quantum efficiency enhancement of midwave infrared nBn photodetectors using one-dimensional plasmonic gratings," Appl. Phys. Lett. **106**(26), 261109 (2015).
14. N. Vanamala, K. C. Santiago, and N. C. Das, "Enhanced MWIR absorption of HgCdTe (MCT) via plasmonic metal oxide nanostructures," AIP Adv. **9**(2), 5054 (2019).
15. Q. Li, Z. Li, N. Li, *et al.*, "High-polarization-discriminating infrared detection using a single quantum well sandwiched in plasmonic micro-cavity," Sci. Rep. **4**(1), 6332 (2014).
16. A. Janaszek, P. Wróbel, R. Kotynski, *et al.*, "Plasmon-enhanced high operating temperature infrared photodetectors," in *Metamaterials XIV* (SPIE, 2023), p. 27.
17. J. Tong, L. Y. M. Tobing, and D. H. Zhang, "Electrically controlled enhancement in plasmonic mid-infrared photodiode," Opt. Express **26**(5), 5452–5460 (2018).
18. Z. Zhou, H. Lin, X. Pan, *et al.*, "Surface plasmon enhanced InAs-based mid-wavelength infrared photodetector," Appl. Phys. Lett. **122**(9), 2267 (2023).
19. S. C. Lee, S. Krishna, Y.-B. Jiang, *et al.*, "Plasmonic-coupled quantum dot photodetectors for mid-infrared photonics," Opt. Express **29**(5), 7145–7157 (2021).
20. S. A. Maier, *Plasmonics. Fundamentals and Applications* (Springer, 2007), p. 21.
21. C. Genet and T. W. Ebbesen, "Light in tiny holes," Nature **445**(7123), 39–46 (2007).
22. Y. Zhong, S. D. Malagari, T. Hamilton, *et al.*, "Review of mid-infrared plasmonic materials," J. Nanophoton **9**(1), 93791 (2015).
23. S. Das, S. Sengupta, G. Jayaswal, *et al.*, "Design of Plasmonic Coupler with Germanium Spacer Layer for Quantum Well Infrared Photodetectors," Plasmonics **18**(1), 1–8 (2023).
24. J. A. Montoya, Z.-B. Tian, S. Krishna, *et al.*, "Ultra-thin infrared metamaterial detector for multicolor imaging applications," Opt. Express **25**(19), 23343–23355 (2017).

Optics EXPRESS

25. A. Pesach, S. Sakr, E. Giraud, *et al.*, "First demonstration of plasmonic GaN quantum cascade detectors with enhanced efficiency at normal incidence," Opt. Express **22**(17), 21069–21078 (2014).
26. J. A. Nolde, E. M. Jackson, M. Kim, *et al.*, "Temperature dependence of quantum efficiency enhancement using plasmonic gratings on nBn detectors with thin absorbers," J. Nanophoton **13**(04), 1 (2019).
27. J. A. Nolde, E. M. Jackson, M. V. Warren, *et al.*, "Back Surface Plasmonic Grating for Increased Quantum Efficiency of nBn Photodetectors with Ultra-Thin Metamorphic InAs0.8Sb0.2 Absorber," IEEE J. Quantum Electron **55**(2), 1–11 (2019).
28. C. Xiang, D. Zhao, C. Zhou, *et al.*, "Three-dimensional measurement module of transverse odd-even combinational Dammann grating," in *Holography, Diffractive Optics, and Applications VIII* (SPIE, 2018), p. 19.
29. X. Cai, Z. Shi, H. Jiang, *et al.*, "Advancing tunable structured light with PT-symmetric dammann grating metasurfaces," Appl. Phys. B **130**(11), 33 (2024).
30. X. Zheng, J. Yang, R. Wang, *et al.*, "Visible light waveband Dammann grating based on all-dielectric metasurface," Appl Opt **61**(9), 2184–2191 (2022).
31. X. Cai, Z. Shi, W. Liu, *et al.*, "Investigation of tunable structured light using bilayer parity-time symmetry Dammann grating metasurfaces," Opt. Laser Technol. **189**(12), 113136 (2025).
32. N. Kinsey, C. DeVault, J. Kim, *et al.*, "Epsilon-near-zero Al-doped ZnO for ultrafast switching at telecom wavelengths," Optica **2**(7), 616 (2015).
33. L. Baldassarre, E. Sakat, J. Frigerio, *et al.*, "Midinfrared Plasmon-Enhanced Spectroscopy with Germanium Antennas on Silicon Substrates," Nano Lett. **15**(11), 7225–7231 (2015).
34. T. Taliercio and P. Biagioni, "Semiconductor infrared plasmonics," Nanophotonics **8**(6), 949–990 (2019).
35. A. Rossetti, H. Hu, T. Venanzi, *et al.*, "Control and enhancement of optical nonlinearities in plasmonic semiconductor nanostructures," Light:Sci. Appl. **14**(1), 192 (2025).
36. G. Perrakis, O. Tsilipakos, G. Kenanakis, *et al.*, "Perfect optical absorption with nanostructured metal films: design and experimental demonstration," Opt. Express **27**(5), 6842–6850 (2019).
37. S. Adachi, *The Handbook on Optical Constants of Metals* (World Scientific Pub., 2012), pp. 68–77.